Journal of Marine Science and Application (2024) 23: 798-811
https://doi.org/10.1007/s11804-024-00470-x

RESEARCH ARTICLE

Ship Propeller Rotation Threshold to Prevent Erosion and Sedimentation in Coastal Waters

Abdul Kadir[1,2], I. Istadi[1,3], Agus Subagio[1,4], I. Iskendar[2], W. Waluyo[2], Abdul Muis[2], Dewi Kartikasari[2], Siti Sadiah[2], A.B Widagdo[5], M.P Helios[6], Mochammad Nasir[7] and N. Nurhadi[7]

Received: 14 October 2023 / Accepted: 01 February 2024

Abstract

The rotation of a ship's propeller can accelerate the water flow around it, which puts pressure on seabed particles. Continuous pressure on the seabed can significantly trigger erosion and sedimentation of coastal waters. Considering the impact that can be caused, the ship's propeller rotation limit needs to be determined to avoid damage to the aquatic ecosystem. This research determines the threshold of ship propeller rotation based on the water flow velocity characteristic. Research has been carried out at the Hydrodynamics Laboratory on several variations of propeller rotation R_{rmp} (r/min) and water depth using empirical approaches, numerical simulations, and scale model experiments. Analysis based on general standard criteria for erosion and sedimentation shows that a propeller with a diameter (D_p) of 1.5 m is safe for propeller rotation at 25 r/min at all water depths. Then, the propeller rotation of 75 r/min is safe for a distance between the propeller axis and the bottom of the water equal to D_p. Meanwhile, rotation at 120 r/min is safe at a minimum distance of 1.5 D_p, and 230 r/min is safe for a minimum distance of 2.0 D_p. The propeller rotation threshold criteria are essential to determining the new under-keel clearance for environmentally friendly ship operations. Threshold values vary based on seabed particle type and water depth.

Keywords Landing craft tank; Water flow velocity; Seabed erosion; Under keel clearance

Article Highlights

- The water flow velocity from propeller rotation must be investigated to determine the effect of shipping on sedimentation processes.
- The propeller's rotation and water depth determine the sedimentation of the seabed.
- This study focuses on determining the suitability of rotating the ship's propellers with the water depth without causing sedimentation.
- The propeller rotation threshold is a reference for environmentally friendly ship operational concepts.

✉ Abdul Kadir
abdkptrim@students.undip.ac.id;
I. Istadi
istadi@che.undip.ac.id

[1] Doctoral Program of Environmental Science, School of Postgraduate Studies, Universitas Diponegoro, Semarang, Central Java 50275, Indonesia

[2] Research Center for Transportation Technology, National Research and Innovation Agency (BRIN), Jakarta 10340, Indonesia

[3] Department of Chemical Engineering, Faculty of Engineering, Universitas Diponegoro, Semarang, Central Java 50275, Indonesia

[4] Department of Physics, Faculty of Science and Mathematics, Universitas Diponegoro, Semarang, Central Java 50275, Indonesia

[5] Research Center for Hydrodynamic Technology, National Research and Innovation Agency (BRIN), Jakarta 10340, Indonesia

[6] Research Center for Energy Conversion and Conservation, National Research and Innovation Agency (BRIN), Jakarta 10340, Indonesia

[7] Directorate of Laboratory Management, Research Facilities, and Science and Technology Park, National Research and Innovation Agency (BRIN), Jakarta 10340, Indonesia

1 Introduction

The propeller's performance mainly determines a ship's operational capability and water mobility. The propeller's rotation changes the shaft torque by accelerating the water flow, producing an axial thrust against the ship (Massey, 2006; Carlton, 2007). The resulting water flow velocity value depends on the propeller's diameter, rotation and thrust coefficient (Hamill et al., 2015). The size and hydrodynamic characteristics of the air bubbles in the water jet from the propeller rotation can influence the quality of the water flow velocity towards the Seabed (Zhang et al., 2023a; 2023b). The water flow velocity can cause significant erosion and suspension of sediment when it reaches the bottom (Kaidi et al., 2021). The closer the propeller is to the seabed, the easier it will cause erosion and sedimentation (Wei & Chiew, 2018; PIANC, 2008). The process of erosion and sedimentation due to propeller rotation has been discussed in previous studies, where there is a direct correlation between propeller rotation and water depth on erosion posture of the seabed including (PIANC, 2008; Hong et al., 2013; Mujal-Colilles et al., 2017; Cui et al., 2019a; 2019b; Schmunk et al., 2023; Ferraro et al., 2023; Cihan et al., 2022). Erosion and sedimentation occur when the water flow velocity causes the seabed shear stress to be greater than the critical shear stress (van Rijn, 2007a). Criti-

cal shear stress is identical to the balance between the force components acting on seabed particles, determining the sediment movement threshold (Yang et al., 2019). Theoretically, single sediment particles moving in water are influenced by static forces such as gravitational and buoyant forces and several dynamic forces such as drag, additional fluid mass, and lift forces (Gotoh & Khayyer, 2016). Several studies, such as those by Mohr (2015), Yao (2019), and British Standard (2003) extensively discuss the critical velocity limit for water flowing to the seabed, the value of which depends on the composition of the particles and the height above the surface of the seabed. Sedimentation can affect the balance of coastal ecosystems and is a significant contributor to the shallowing of shipping lanes, disrupting navigation systems, affecting under-keel clearance (UKC) standards and ship manoeuvring (Scully & Young, 2021; Oud & Bedos, 2022).

Erosion and sedimentation are susceptible to being caused by ships with small drafts, such as Landing Craft Tank (LCT) ships. LCT ships have high mobility capabilities, can operate in shallow waters, reach remote areas, navigate bays and rivers, and anchor directly in small ports or open beaches. Due to good mobility considerations, LCT ships are recommended to support LNG distribution to power plants on small islands and remote areas in Eastern Indonesia (Legawa et al., 2020; Abdillah et al., 2021; The Ministry of Energy and Mineral Resources of Republic of Indonesia, 2021). There is no generally agreed standard for limiting the water flow velocity caused by ship propellers as a trigger for erosion for all seabed conditions (Kadir et al., 2022). This research investigates the propeller rotation threshold on the LCT ship. The water flow velocity caused by the propeller rotation was investigated at several depths to represent the seabed. Each depth has a different propeller rotation threshold depending on the type of seabed particles. Propeller rotation threshold data is an essential variable for determining environmentally friendly UKC, as depicted in the automation system schematic in Figure 1. Inaccurate determination of UKC can impact safety, economy and environmental damage (PIANC, 1985).

2 Methods

This research focuses on the water flow velocity of the LCT ship's propeller rotation. The propeller's technical data are given in Figure 2 and Table 1.

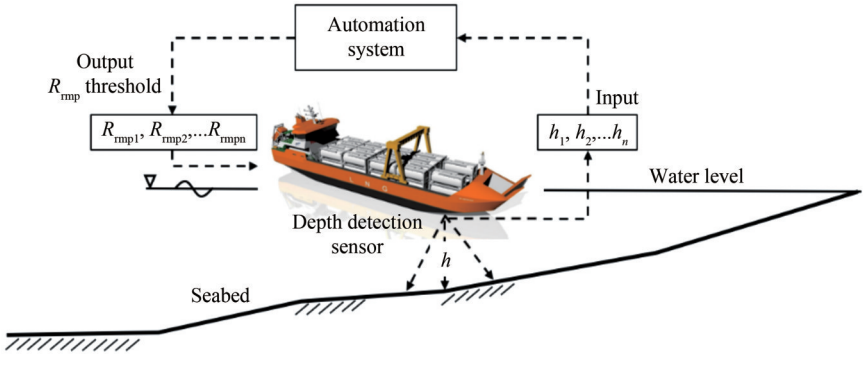

Figure 1 Concept for environmentally friendly ship operations (Kadir et al., 2022)

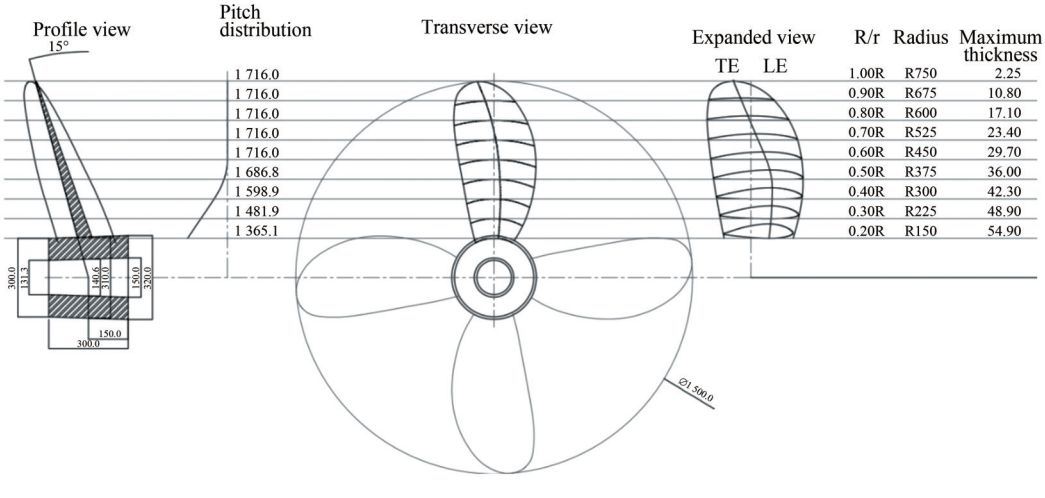

Figure 2 Propeller projection of LCT type mini LNG (units: mm)

Table 1 Variables dimension of propeller

Scale	Diameter D_p (m)	Pitch at the diameter ratio P/D_p	Expanded blade area ratio A_E/A_0	Number of blades Z (blade)
Full scale	1.499	1.144	0.400	4
Model scale*	0.131	1.144	0.400	4

Note:* represents scale factor: 1:11.428

Water flow velocity was investigated using three approaches. Empirical equations were used in the initial investigation, then verified using numerical simulations, and finally validated using model scale experiments in a hydrodynamic laboratory. The investigation assumed the ship was anchored on an open beach, and the ship's speed was close to zero; hence, the effect of turbulent waves on the ship's hull could be neglected. The steering effect was also ignored, considering that the steering angle at the zero-degree position does not influence the vertical posture of the axial velocity of the water flow (G. A. Hamill & Johnston, 1993).

Vertical investigations were conducted at four depths from the propeller axle, namely, 0.5, 1.0, 1.5 and 2.0 D_p, as shown in Figure 3. The conversion of depth values to UKC is presented in Table 2. Horizontal investigations were performed in two zones, namely, the zone of flow establishment (ZFE) in range $0 < x/D_p \leqslant 3.25$ and the zone of established flow (ZEF), as shown in Figure 4. The ZFE begins from the centre of the propeller axis to the point $x/D_p = 2.6$ (Fuehrer et al., 1987) (Blaauw & van de Kaa, 1978). Several studies have revealed that $x/D_p = 2.77$ (Verhey, 1983) and $x/D_p = 3.25$ (Lam et al., 2011), where x is the horizontal distance, and D_p is the propeller diameter.

In the range $0 < x/D_p < 0.35$, the most remarkable water flow velocity, called efflux velocity (V_o), is observed in the middle of the radius of the propeller blade. In the range $0.35 < x/D_p < 3.25$, V_o gradually shifts and converges to form one peak of maximum axial velocity (V_{max}) on the propeller axis line, which signifies a stable flow zone formation. $V_{x,r}$ indicate the flow velocity at a distance r from the propeller axis line.

2.1 Empirical approach

Previous research presented the typical step for obtaining the water flow velocity value component due to propeller rotation for single and twin propellers (Lam et al., 2011; Jiang et al., 2019). The velocity value in each zone can be known based on the empirical equations in Table 3.

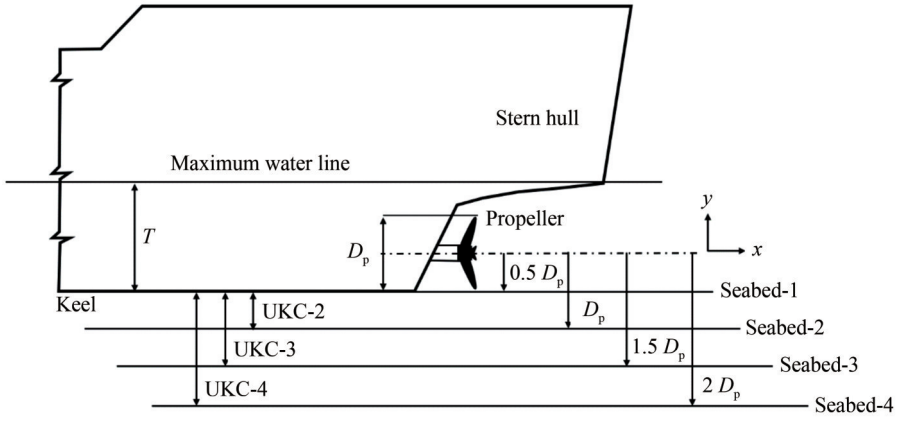

Figure 3 Propeller position and water depth level investigation

Table 2 Equivalent value of depth parameters in full-scale

Ship draught T (m)	Propeller diameter D_p (m)	Propeller axis to depth target y/D_p	Under-keel clearance UKC (m)	Water depth h (m)	Ratio UKC/T	Ratio T/h
(1)	(2)	(3)	(4) = (2) × (3) − ((2)/2)	(5) = (1) + (4)	(6) = (4)/(1)	(7) = (1)/(5)
2.5	1.5	0.5	0	2.50	0	1.0
2.5	1.5	1.0	0.75	3.25	0.3	0.8
2.5	1.5	1.5	1.50	4.00	0.6	0.6
2.5	1.5	2.0	2.25	4.75	0.9	0.5

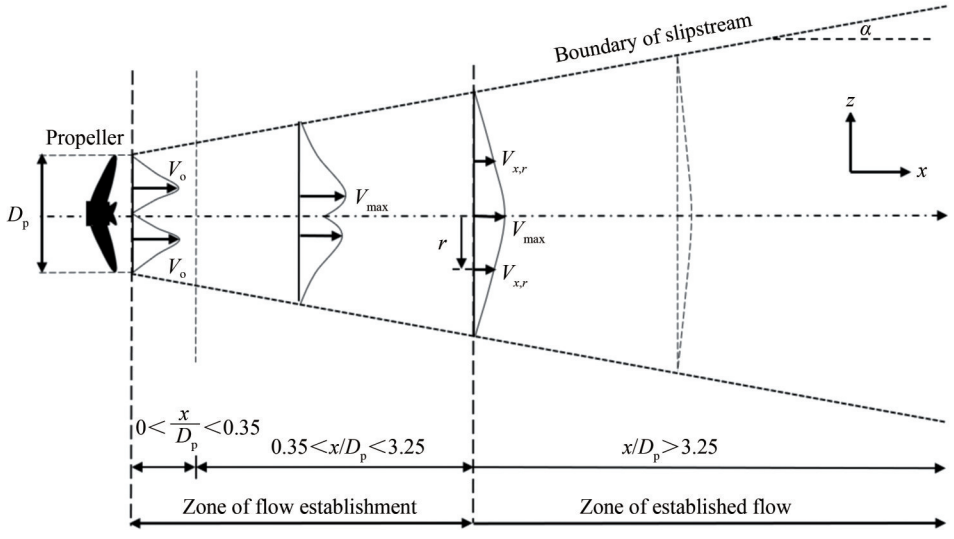

Figure 4 Plan view of the water flow zones division of the propeller system

Table 3 Empirical equations for water flow velocity

Zone of flow establishment (ZFE)		Zone of established flow (ZEF)
$0 < x/D < 0.35$	$0.35 < x/D < 3.25$	$x/D > 3.25$
By Fuehrer (Fuehrer et al., 1987) $V_o = 1.59nD_p\sqrt{C_t}$ (1) where n is the revolution of the propeller (s^{-1}), and C_t is the thrust coefficient	By Stewart (Jiang et al., 2019) $\frac{V_{max}}{V_o} = 1.017\,2 - 0.183\,5\left(\frac{x}{D}\right)$ (6)	By Fuehrer (Fuehrer et al., 1987) $\frac{V_{x,r}}{V_{max}} = e^{\left[-22.2\left(\frac{r}{X}\right)^2\right]}$ (11)
By Hamill (Hamill, 1988) $V_o = 1.33nD_p\sqrt{C_t}$ (2)	By Verhey (Verhey, 1983) $\frac{V_{max}}{V_o} = 1.275\left(\frac{x}{D}\right)^{-0.7}$; $(1.5 < x/D)$ (7)	By Fuehrer (Fuehrer et al., 1987) $\frac{V_{max}}{V_o} = 2.6\left(\frac{x}{D}\right)^{-1.0}$ (12)
By Stewart in (Lam et al., 2011) $V_o = \varsigma nD\sqrt{C_t}$ (3) where $\varsigma = D^{-0.068\,6}\left(\frac{P}{D}\right)^{1.519} BAR^{-0.323}$ BAR is the blade area ratio, and P/D is the pitch ratio of the propeller.	By Lam (Lam et al., 2011) $\frac{V_{max}}{V_o} = 1 - 0.159\,2\left(\frac{x}{D}\right)$ (8)	By Blaauw (Blaauw and van de Kaa, 1978) $\frac{V_{max}}{V_o} = 2.8\left(\frac{x}{D}\right)^{-1.0}$ (13)
By Hashmi (Hashmi, 1993) $V_o = E_o nD\sqrt{C_t}$ (4) where $E_o = \left(\frac{D}{D_h}\right)^{-0.403} C_t^{-1.79} BAR^{0.744}$ D_h are propeller hub diameters	By Hamill (Hamill, Kee, and Ryan, 2015) $\frac{V_{max}}{V_o} = 1.51 - 0.175\left(\frac{x}{D}\right) - 0.46P'$ (9) $P' = \left(\frac{P}{D}\right)$	By Blaauw (Blaauw and van de Kaa, 1978) $\frac{V_{x,r}}{V_{max}} = e^{\left[-15.4\left(\frac{r}{X}\right)^2\right]}$ (14)
		By Bergerl (Berger et al., 1981) $\frac{V_{max}}{V_o} = 1.025\left(\frac{x}{D}\right)^{-0.6}$ (15)
By Hamill (Hamill, Kee, and Ryan, 2015) $V_o = 1.22n^{1.01} D_p^{0.84} C_t^{0.62}$ (5)	By Hamill (Hamill, 1988) $\frac{V_{x,r}}{V_{max}} = \mathrm{EXP}\left[-\frac{1}{2}\frac{\left(r - R_{mo}\right)^2}{\sigma^2}\right]$ (10) $\sigma = 0.5R_{mo}$; $(x/D < 0.5)$ $\sigma = \frac{1}{2}R_{mo} + 0.75\left(X - \frac{D}{2}\right)$; $(x/D > 0.5)$	By Stewart (Jiang et al., 2019) $\frac{V_{max}}{V_o} = 0.543 - 0.028\,1\left(\frac{x}{D}\right)$ (16) By Hashmi (Hashmi, 1993) $\frac{V_{max}}{V_o} = 0.638e^{\left(-0.097\left(\frac{x}{D}\right)\right)}$ (17)
		By Hamill (Hamill, Kee, and Ryan, 2015) $\frac{V_{max}}{V_o} = 0.964 - 0.039\left(\frac{x}{D}\right) - 0.344P'$ (18)

Note: $D = D_p$ (propeller's diameter)

2.2 Numerical simulation by computational fluid dynamic fluent using ANSYS Fluent Software

The ANSYS Fluent 18.0 (ANSYS Fluent, 2018) is used to analyse the flow by assuming a 1:1 scale propeller design with a simulation domain, as shown in Figure 5.

The simulation focused on the non-interference zone, taking one propeller as a sample. Domain boundary data are $+X = 21$ m $(14D_p)$, $+Y = 2.25$ m $(1.5D_p)$, $+Z = 2.70$ m $(1.8D_p)$, $-X = 1.50$ m $(1.0D_p)$, $-Y = 4.50$ m $(3D_p)$, $-Z = 2.70$ m $(1.8D_p)$. The simulation approach is a 3D steady state with symmetry on the x-y plane. The domain consists of a propeller zone and a water zone with a 998 kg/m^3 water density. The multi-reference frame (MRF) was applied in both domains. Both inlet and outlet are defined as pressure inlet and outlet, respectively, and the clockwise propeller rotation is set between 100–400 r/min. The Realistic $k-\varepsilon$ turbulence model and the pressure coupling-second order method were selected due to the accuracy among turbulence models.

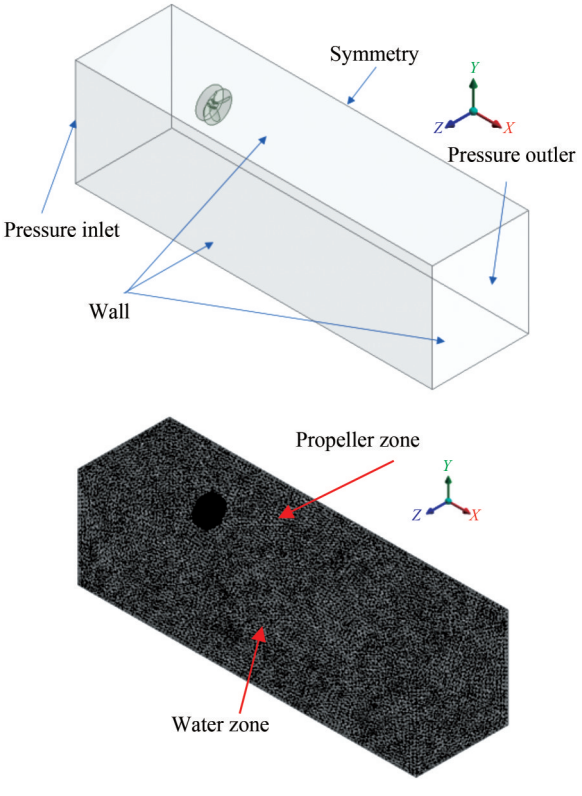

Figure 5 Propeller simulation domain and meshing

Five element sizes, namely, 0.1, 0.2, 0.4, 0.8, and 1.2 mm, tested to enhance the number of elements, were adequate for the simulation, as shown in Figure 6. The velocity of water through the propeller domain was selected as a benchmark. Increasing the number of mesh does not affect the value of water velocity entering the propeller zone. The lowest relative error was found to be about 0.56%, and the highest relative error was 2.12%. Hence, the average relative error was about 1.18%.

Figure 7 visualises the trend of water velocity by the CFD model, which has a pattern of agreement with the experimental measurement. The CFD model predicted the velocity of water entering the inlet propeller zone with an accuracy of less than 7.6%.

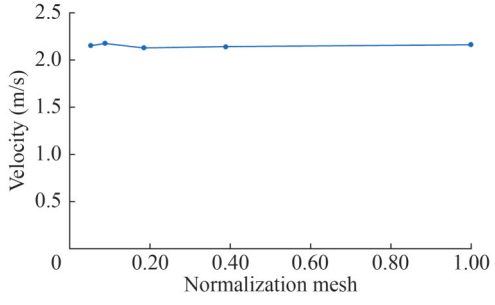

Figure 6 Mesh independency

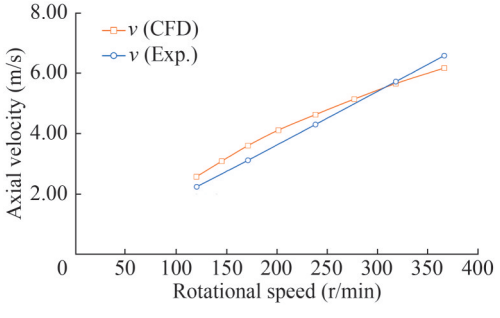

Figure 7 Validation of water velocity entering the propeller zone

2.3 Experiment setup with model scale

A model scale experiment was performed in a hydrodynamic laboratory, where the tank has a length (L) of 234 m, a width (B) of 11 m and a depth (T) of 5.5 m. Considering the size and features of the test tank, the model scale used to obtain the size of the propeller model is 1:11.428, as shown in Table 1. The scale effect on viscosity can be neglected if the Reynold number of the Propeller (Re_{prop}) is more significant than 7×10^4 and the Reynold number of the water flow (Re_{flow}) exceeds 3×10^3 (Verhey, 1983). The Reynold number equation is expressed as follows:

$$Re_{prop} = \frac{nL_m D_p}{v} \tag{19}$$

$$Re_{flow} = \frac{V_o D_p}{v} \tag{20}$$

where V_o is the efflux velocity, D_p is the propeller diameter, v is the water kinematic viscosity (8.040E-07 (m^2/s)) at 30 °C (Crittenden et al., 2012), n is propeller rotation per second. L_m is the characteristic length of the propeller that

is derived by Equation (21) (Blaauw & van de Kaa, 1978) :

$$L_m = \beta \cdot D_p \cdot \pi \cdot \left\{2N\left(1 - \frac{D_h}{D_p}\right)\right\}^{-1} \quad (21)$$

where β is the blade area ratio, N is the number of propeller blades, and D_h is the propeller hub diameter.

Based on Equations (19) and (20), the obtained $Re_{prop} = 6 \times 10^7 > 7 \times 10^4$ and $Re_{flow} = 5.3 \times 10^6 > 3 \times 10^3$.

The scheme used in the analysis of the velocity of water flows from the model scale of the propeller in the hydrodynamic laboratory experimental tank is shown in Figures 8(a) and 8(b). Flow velocity was quantified using a portable velocity meter with a measurement capacity of 1–400 cm/s with an error rate of ⩽1.5%. In the measurement, the velocity meter blade was rotated by the water flow, the sensor signal generated the revolution signal as shown in Figure 9, and the flow velocity can be calculated by Equation (22):

$$V = \frac{KN}{T} + C\,(\mathrm{m/s}) \quad (22)$$

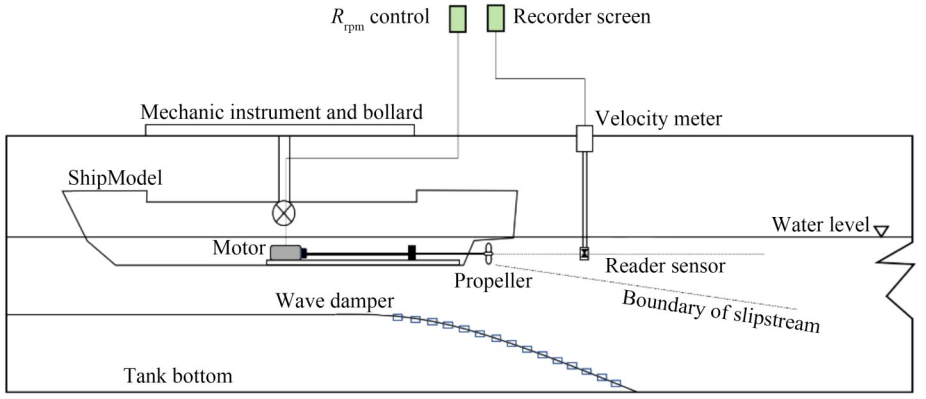

(a) Experiment setup scheme

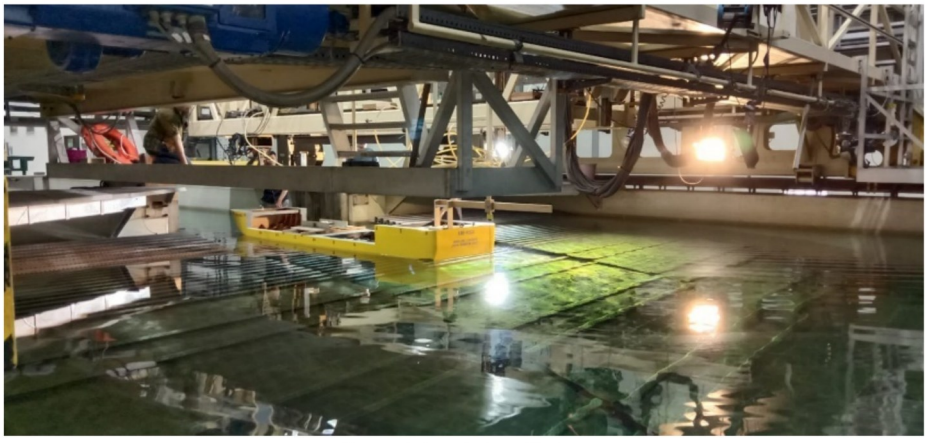

(b) Model scale installation

Figure 8 Experiment setup scheme and the model scale installation

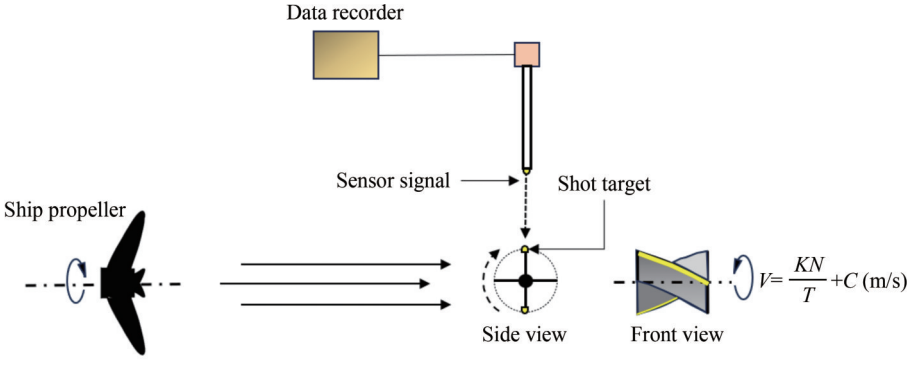

Figure 9 The working principle of the measuring instrument

where V is the mean flow velocity, K is the screw pitch, C is the constant of the velocity meter, T is the amount of time, and N is the number of signals during T. The measurement results were converted to the actual value using the scale factor.

3 Water flow velocity initiates erosion and sedimentation

The V_{max} of the water flow caused by the propeller rotation is distributed as the radial velocity ($V_{x,r}$) at a distance r from the propeller axis, as presented in Figure 10(a). $V_{x,r}$ reaching the seabed causes the shear stress of θ flow and friction velocity u_*. Initial motion in steady flow occurs when the dimensionless bed-shear stress θ is more substantial than a threshold θ_{cr} ($\theta > \theta_{cr}$), (van Rijn, 2007b). Seabed particles tend to maintain their position due to the work of gravity (G) and cohesion forces (F_c), and start to move when the critical stress limit is exceeded due to the work of lift force (F_L) and drag force (F_D), as illustrated in Figure 10(b). The seabed particle type and size category are given in Table 4.

The water flow velocity that starts erosion can be identified based on the Hjulstrom diagram as a function of the water flow velocity and the grain size of the Seabed (Hjulström, 1955). In addition, there is a Shield curve as a function of the Shield parameter and Reynolds number (Shields, 1936). Hjulstrom and Shield's diagrams have been the primary reference for several authors in decades, such as (Miedema, 2013; Corcoran et al., 2016; Huai et al., 2019; Van Rijn & Kroon, 1993; Soulsby, 1997), which provide iteration of criterion limits in the form of Equation (23).

$$\theta = \frac{\tau_{cr}}{(\rho_s - \rho) g d} \tag{23}$$

where τ_{cr} is critical bed shear stress at initial motion $\tau_{cr} = \rho u_*^2$, ρ (1 000 kg/m^3) is fluid, ρ_s is particle density, d is median particle size, g is the acceleration due to gravity, and u_* is friction velocity.

$$u_* = (ghI)^{1/2} \tag{24}$$

where h is water depth, I is potential energy slope $I = (V \cdot n/h^{2/3})^2$, V is water flow velocity, and n is manning coefficient.

Numerous experiments have performed the θ_{cr} value as a function of D_*. van Rijn (2007b) represented the relationship between θ_{cr} and D_* in Equations (25a) and (25b)

$$\theta_{cr} = 0.115 (D_*)^{-0.5}, \ D_* < 4 \tag{25a}$$

$$\theta_{cr} = 0.14 (D_*)^{-0.64}, \ 4 \leqslant D_* < 10 \tag{25b}$$

where θ_{cr} is the critical shear stress, and D_* is the modified grain Reynolds number.

$$D_* = \left[\frac{g(s-1)}{v^2} \right]^{1/3} d \tag{26}$$

where $s = \rho_s / \rho$ and v is the viscosity of the fluid.

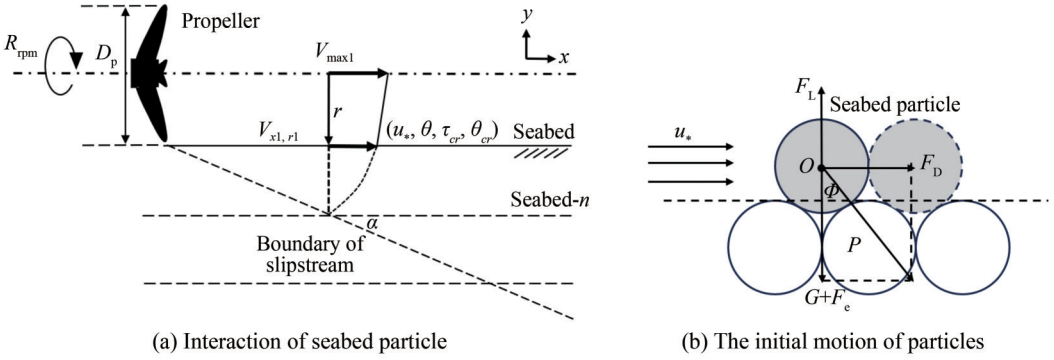

(a) Interaction of seabed particle (b) The initial motion of particles

Figure 10 Initial parameters of seabed particle motion

Table 4 Variation of the seabed particles diameter in (mm)

Size category	Particle type				
	Clay	Silt	Sand	Gravel	Cobbles
Fine	< 0.002	0.002 0–0.006 0	0.062 5–0.200 0	2.0–6.0	> 60
Medium		0.006 0–0.020 0	0.200 0–0.600 0	6.0–20	
Coarse		0.020 0–0.062 5	0.600 0–2.000 0	20–60	

4 Results and discussion

4.1 Trend of water flow velocity

At a distance of $0 < x/D_p < 0.35$, the maximum efflux velocity component (V_o) increases with increasing propeller rotation, where the simulation and experimental results have almost the same value, as shown in Figure 11(a). The velocity decay (V_{max}/V_o) of the model scale experiment follows the trend of numerical CFD simulation and previous research calculations, where a significant reduction in the zone of flow establishment is shown in Figure 11(b).

The velocity decay slopes linearly in the zone of established flow where at $x/D_p > 7$, the value of V_{max}/V_o tends to be the same, apart from the fact that the flow has entered the interferent zone for Twin Propeller System (Kadir et al., 2023), it can also be affected because the distance between the propeller axis and the bottom of the water is much greater than the distance between the axis and the surface of the water (Blaauw & van de Kaa, 1978).

The flow velocity characteristics tend to form one peak and concentrate around the propeller rotation axis. The vertical flow velocity characteristic posture in section x/D_p = 0.35 forms two velocity peaks, as shown in Figure 11(c), and the maximum velocity occurs around half of the propeller radius. Figure 11(d) is the flow velocity posture at the x/D_p = 3.5 section or the initial zone of established flow. The measurement results are generally more excellent than empirical calculations but smaller than numerical CFD simulation results.

The approaches' results differ due to the influence of the properties used; where the empirical approach uses coefficient factors, the numerical simulation considers scale factors for environmental characteristics, as in Figure 12. For the model experiments, actual field characteristics are used to make the results closer to the real environmental condition.

4.2 Water flow velocity in variations of propeller rotation

Figure 13 and Table 5 present the accumulated results of the investigation of water flow velocity caused by the propeller rotation at variations in the vertical distance from the propeller axis and rotation variations of 25 to 366 r/min. Figures 13(a) and 13(b) reveal four conditions where the flow velocity is greater than 1 m/s with a maximum velocity of 6 m/s; Figure 13(c) shows three conditions where the flow velocity is greater than 1 m/s with a maximum value of 3.5 m/s. Figure 13(d) presents only 1 condition where

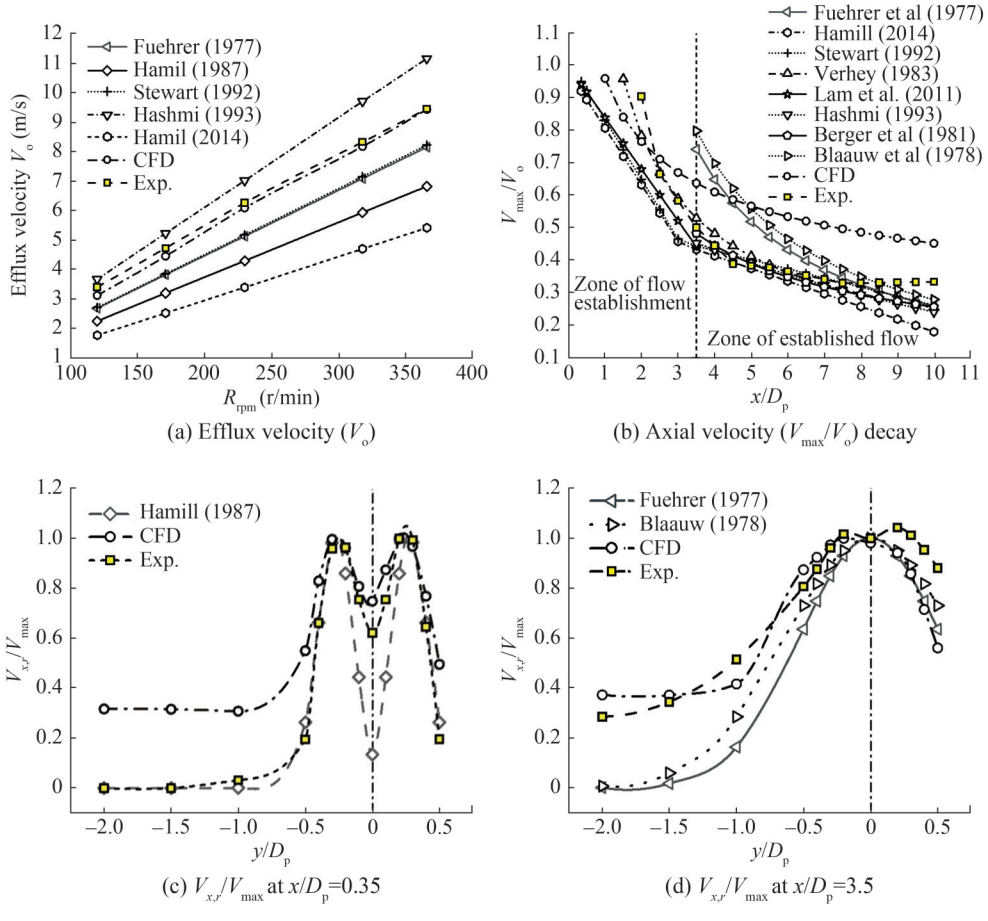

Figure 11 Water flow velocity trend

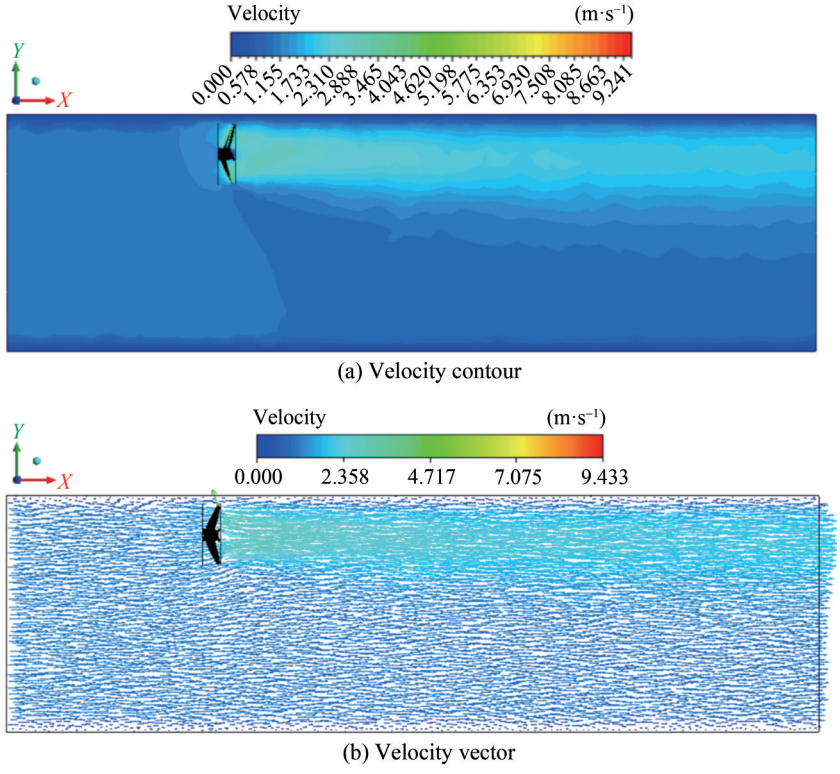

Figure 12 Water flow velocity contour and vector

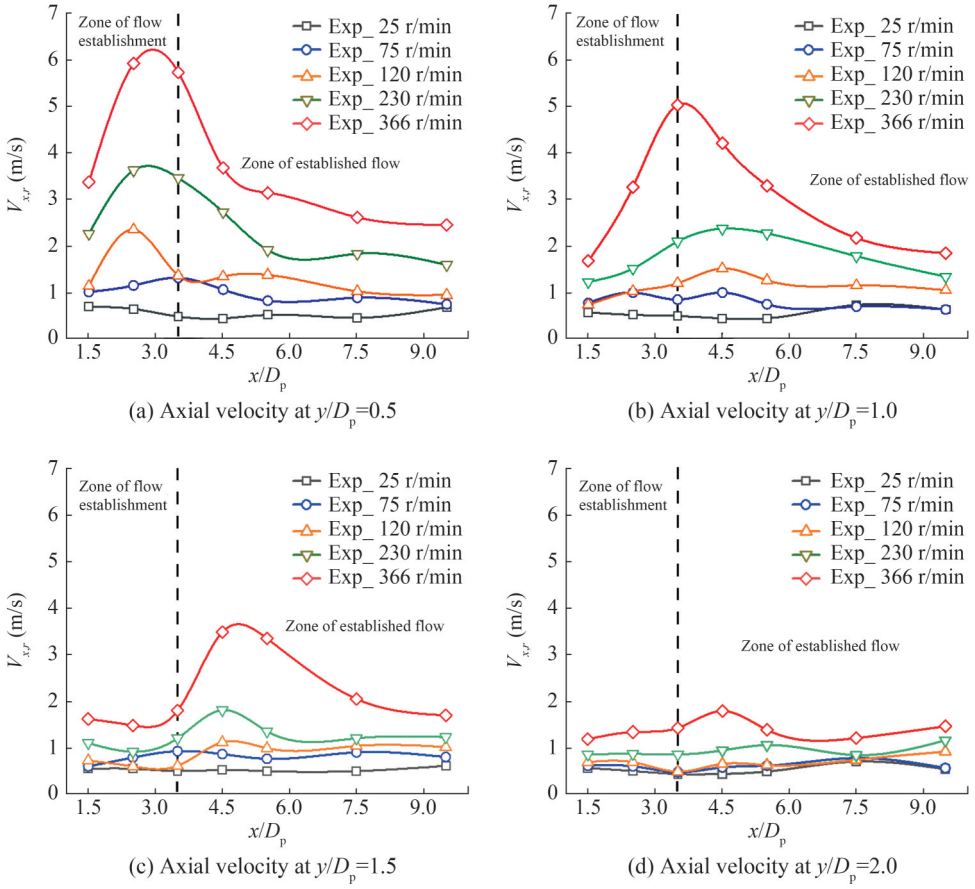

Figure 13 Water flow velocity in r/min variation

Table 5 Summary of shear stress and critical shear stress based on seabed particles

(a) Y=0.5 D_p

Propeller rotation (r/min)	Measured velocity V (m/s)	U_* (m/s)	τ_{cr} (kg/m^2)	Clay			Silt			Sand			Gravel		
				θ (kg/m^2)	θ_{cr} (kg/m^2)	Stability control	θ (kg/m^2)	θ_{cr} (kg/m^2)	Stability control	θ (kg/m^2)	θ_{cr} (kg/m^2)	Stability control	θ (kg/m^2)	θ_{cr} (kg/m^2)	Stability control
25	0.5	2.47 E-03	6.08 E-03	3.80 E-01	5.53 E-01	$\theta<\theta_{cr}$	1.22 E-02	1.07 E-01	$\theta<\theta_{cr}$	1.27 E-03	2.72 E-02	$\theta<\theta_{cr}$	3.04 E-04	1.20 E-02	$\theta<\theta_{cr}$
75	0.5	2.47 E-03	6.08 E-03	3.80 E-01	5.53 E-01	$\theta<\theta_{cr}$	1.22 E-02	1.07 E-01	$\theta<\theta_{cr}$	1.27 E-03	2.72 E-02	$\theta<\theta_{cr}$	3.04 E-04	1.20 E-02	$\theta<\theta_{cr}$
	1.0	4.93 E-03	2.43 E-02	1.52 E+00	5.53 E-01	$\theta>\theta_{cr}$ erodible	4.87 E-02	1.07 E-01	$\theta<\theta_{cr}$	5.07 E-03	2.72 E-02	$\theta<\theta_{cr}$	1.22 E-03	1.20 E-02	$\theta<\theta_{cr}$
120	1.0	4.93 E-03	2.43 E-02	1.52 E+00	5.53 E-01	$\theta>\theta_{cr}$ erodible	4.87 E-02	1.07 E-01	$\theta<\theta_{cr}$	5.07 E-03	2.72 E-02	$\theta<\theta_{cr}$	1.22 E-03	1.20 E-02	$\theta<\theta_{cr}$
	2.0	9.87 E-03	9.74 E-02	6.08 E+00	5.53 E-01	$\theta>\theta_{cr}$ erodible	1.95 E-01	1.07 E-01	$\theta>\theta_{cr}$ erodible	2.03 E-02	2.72 E-02	$\theta<\theta_{cr}$	4.87 E-03	1.20 E-02	$\theta<\theta_{cr}$
230	2.0	9.87 E-03	9.74 E-02	6.08 E+00	5.53 E-01	$\theta>\theta_{cr}$ erodible	1.95 E-01	1.07 E-01	$\theta>\theta_{cr}$ erodible	2.03 E-02	2.72 E-02	$\theta<\theta_{cr}$	4.87 E-03	1.20 E-02	$\theta<\theta_{cr}$
	4.0	1.97 E-02	3.89 E-01	2.43 E+01	5.53 E-01	$\theta>\theta_{cr}$ erodible	7.79 E-01	1.07 E-01	$\theta>\theta_{cr}$ erodible	8.11 E-02	2.72 E-02	$\theta>\theta_{cr}$ erodible	1.95 E-02	1.20 E-02	$\theta>\theta_{cr}$ erodible
366	4.0	1.97 E-02	3.89 E-01	2.43 E+01	5.53 E-01	$\theta>\theta_{cr}$ erodible	7.79 E-01	1.07 E-01	$\theta>\theta_{cr}$ erodible	8.11 E-02	2.72 E-02	$\theta>\theta_{cr}$ erodible	1.95 E-02	1.20 E-02	$\theta>\theta_{cr}$ erodible
	6.0	2.96 E-02	8.76 E-01	5.48 E+01	5.53 E-01	$\theta>\theta_{cr}$ erodible	1.75 E+00	1.07 E-01	$\theta>\theta_{cr}$ erodible	1.83 E-01	2.72 E-02	$\theta>\theta_{cr}$ erodible	4.38 E-02	1.20 E-02	$\theta>\theta_{cr}$ erodible

(b) Y=1.0 D_p

Propeller rotation (r/min)	Measured velocity V (m/s)	U_* (m/s)	τ_{cr} (kg/m^2)	Clay			Silt			Sand			Gravel		
				θ (kg/m^2)	θ_{cr} (kg/m^2)	Stability control	θ (kg/m^2)	θ_{cr} (kg/m^2)	Stability control	θ (kg/m^2)	θ_{cr} (kg/m^2)	Stability control	θ (kg/m^2)	θ_{cr} (kg/m^2)	Stability control
25	0.5	1.66 E-03	2.77 E-03	1.73 E-01	5.53 E-01	$\theta<\theta_{cr}$	5.54 E-03	1.07 E-01	$\theta<\theta_{cr}$	5.77 E-04	2.72 E-02	$\theta<\theta_{cr}$	1.38 E-04	1.20 E-02	$\theta<\theta_{cr}$
75	0.5	1.66 E-03	2.77 E-03	1.73 E-01	5.53 E-01	$\theta<\theta_{cr}$	5.54 E-03	1.07 E-01	$\theta<\theta_{cr}$	5.77 E-04	2.72 E-02	$\theta<\theta_{cr}$	1.38 E-04	1.20 E-02	$\theta<\theta_{cr}$
	1.0	3.33 E-03	1.11 E-02	6.92 E-01	5.53 E-01	$\theta>\theta_{cr}$ erodible	2.22 E-02	1.07 E-01	$\theta<\theta_{cr}$	2.31 E-03	2.72 E-02	$\theta<\theta_{cr}$	5.54 E-04	1.20 E-02	$\theta<\theta_{cr}$
120	1.0	3.33 E-03	1.11 E-02	6.92 E-01	5.53 E-01	$\theta>\theta_{cr}$ erodible	2.22 E-02	1.07 E-01	$\theta<\theta_{cr}$	2.31 E-03	2.72 E-02	$\theta<\theta_{cr}$	5.54 E-04	1.20 E-02	$\theta<\theta_{cr}$
	1.5	4.99 E-03	2.49 E-02	1.56 E+00	5.53 E-01	$\theta>\theta_{cr}$ erodible	4.98 E-02	1.07 E-01	$\theta<\theta_{cr}$	5.19 E-03	2.72 E-02	$\theta<\theta_{cr}$	1.25 E-03	1.20 E-02	$\theta<\theta_{cr}$
230	1.5	4.99 E-03	2.49 E-02	1.56 E+00	5.53 E-01	$\theta>\theta_{cr}$ erodible	4.98 E-02	1.07 E-01	$\theta<\theta_{cr}$	5.19 E-03	2.72 E-02	$\theta<\theta_{cr}$	1.25 E-03	1.20 E-02	$\theta<\theta_{cr}$
	2.5	8.32 E-03	6.92 E-02	4.33 E+00	5.53 E-01	$\theta>\theta_{cr}$ erodible	1.38 E-01	1.07 E-01	$\theta>\theta_{cr}$ erodible	1.44 E-02	2.72 E-02	$\theta<\theta_{cr}$	3.46 E-03	1.20 E-02	$\theta<\theta_{cr}$
366	2.5	8.32 E-03	6.92 E-02	4.33 E+00	5.53 E-01	$\theta>\theta_{cr}$ erodible	1.38 E-01	1.07 E-01	$\theta>\theta_{cr}$ erodible	1.44 E-02	2.72 E-02	$\theta<\theta_{cr}$	3.46 E-03	1.20 E-02	$\theta<\theta_{cr}$
	5.0	1.66 E-02	2.77 E-01	1.73 E+01	5.53 E-01	$\theta>\theta_{cr}$ erodible	5.54 E-01	1.07 E-01	$\theta>\theta_{cr}$ erodible	5.77 E-02	2.72 E-02	$\theta>\theta_{cr}$ erodible	1.38 E-02	1.20 E-02	$\theta>\theta_{cr}$ erodible

Table 5 Summary of shear stress and critical shear stress based on seabed particles (continuous)

(c) Y=1.5 D_p

Propeller rotation (r/min)	Measured velocity V (m/s)	U_* (m/s)	τ_{cr} (kg/m^2)	Clay			Silt			Sand			Gravel		
				θ (kg/m^2)	θ_{cr} (kg/m^2)	Stability control	θ (kg/m^2)	θ_{cr} (kg/m^2)	Stability control	θ (kg/m^2)	θ_{cr} (kg/m^2)	Stability control	θ (kg/m^2)	θ_{cr} (kg/m^2)	Stability control
25	0.5	2.47 E-03	6.08 E-03	3.80 E-01	5.53 E-01	$\theta<\theta_{cr}$	1.22 E-02	1.07 E-01	$\theta<\theta_{cr}$	1.27 E-03	2.72 E-02	$\theta<\theta_{cr}$	3.04 E-04	1.20 E-02	$\theta<\theta_{cr}$
75	0.5	2.47 E-03	6.08 E-03	3.80 E-01	5.53 E-01	$\theta<\theta_{cr}$	1.22 E-02	1.07 E-01	$\theta<\theta_{cr}$	1.27 E-03	2.72 E-02	$\theta<\theta_{cr}$	3.04 E-04	1.20 E-02	$\theta<\theta_{cr}$
	0.8	1.95 E-03	3.80 E-03	2.38 E-01	5.53 E-01	$\theta<\theta_{cr}$	7.61 E-03	1.07 E-01	$\theta<\theta_{cr}$	7.92 E-04	2.72 E-02	$\theta<\theta_{cr}$	1.90 E-04	1.20 E-02	$\theta<\theta_{cr}$
120	0.8	1.95 E-03	3.80 E-03	2.38 E-01	5.53 E-01	$\theta<\theta_{cr}$	7.61 E-03	1.07 E-01	$\theta<\theta_{cr}$	7.92 E-04	2.72 E-02	$\theta<\theta_{cr}$	1.90 E-04	1.20 E-02	$\theta<\theta_{cr}$
	1.0	2.44 E-03	5.94 E-03	3.71 E-01	5.53 E-01	$\theta<\theta_{cr}$	1.19 E-02	1.07 E-01	$\theta<\theta_{cr}$	1.24 E-03	2.72 E-02	$\theta<\theta_{cr}$	2.97 E-04	1.20 E-02	$\theta<\theta_{cr}$
230	1.0	2.44 E-03	5.94 E-03	3.71 E-01	5.53 E-01	$\theta<\theta_{cr}$	1.19 E-02	1.07 E-01	$\theta<\theta_{cr}$	1.24 E-03	2.72 E-02	$\theta<\theta_{cr}$	2.97 E-04	1.20 E-02	$\theta<\theta_{cr}$
	2.0	4.88 E-03	2.38 E-02	1.49 E+00	5.53 E-01	$\theta>\theta_{cr}$ erodible	4.75 E-02	1.07 E-01	$\theta<\theta_{cr}$	4.95 E-03	2.72 E-02	$\theta<\theta_{cr}$	1.19 E-03	1.20 E-02	$\theta<\theta_{cr}$
366	2.0	4.88 E-03	2.38 E-02	1.49 E+00	5.53 E-01	$\theta>\theta_{cr}$ erodible	4.75 E-02	1.07 E-01	$\theta<\theta_{cr}$	4.95 E-03	2.72 E-02	$\theta<\theta_{cr}$	1.19 E-03	1.20 E-02	$\theta<\theta_{cr}$
	3.5	8.53 E-03	7.28 E-02	4.55 E+00	5.53 E-01	$\theta>\theta_{cr}$ erodible	1.46 E-01	1.07 E-01	$\theta>\theta_{cr}$ erodible	1.52 E-02	2.72 E-02	$\theta<\theta_{cr}$	3.64 E-03	1.20 E-02	$\theta<\theta_{cr}$

(d) Y=2.0 D_p

Propeller rotation (r/min)	Measured velocity V (m/s)	U_* (m/s)	τ_{cr} (kg/m^2)	Clay			Silt			Sand			Gravel		
				θ (kg/m^2)	θ_{cr} (kg/m^2)	Stability control	θ (kg/m^2)	θ_{cr} (kg/m^2)	Stability control	θ (kg/m^2)	θ_{cr} (kg/m^2)	Stability control	θ (kg/m^2)	θ_{cr} (kg/m^2)	Stability control
25	0.5	9.42 E-04	8.87 E-04	5.54 E-02	5.53 E-01	$\theta<\theta_{cr}$	1.77 E-03	1.07 E-01	$\theta<\theta_{cr}$	1.85 E-04	2.72 E-02	$\theta<\theta_{cr}$	4.44 E-05	1.20 E-02	$\theta<\theta_{cr}$
75	0.5	9.42 E-04	8.87 E-04	5.54 E-02	5.53 E-01	$\theta<\theta_{cr}$	1.77 E-03	1.07 E-01	$\theta<\theta_{cr}$	1.85 E-04	2.72 E-02	$\theta<\theta_{cr}$	4.44 E-05	1.20 E-02	$\theta<\theta_{cr}$
	0.7	1.32 E-03	1.74 E-03	1.09 E-01	5.53 E-01	$\theta<\theta_{cr}$	3.48 E-03	1.07 E-01	$\theta<\theta_{cr}$	3.62 E-04	2.72 E-02	$\theta<\theta_{cr}$	8.69 E-05	1.20 E-02	$\theta<\theta_{cr}$
120	0.7	1.32 E-03	1.74 E-03	1.09 E-01	5.53 E-01	$\theta<\theta_{cr}$	3.48 E-03	1.07 E-01	$\theta<\theta_{cr}$	3.62 E-04	2.72 E-02	$\theta<\theta_{cr}$	8.69 E-05	1.20 E-02	$\theta<\theta_{cr}$
	1.0	1.88 E-03	3.55 E-03	2.22 E-01	5.53 E-01	$\theta<\theta_{cr}$	7.10 E-03	1.07 E-01	$\theta<\theta_{cr}$	7.39 E-04	2.72 E-02	$\theta<\theta_{cr}$	1.77 E-04	1.20 E-02	$\theta<\theta_{cr}$
230	1.0	1.88 E-03	3.55 E-03	2.22 E-01	5.53 E-01	$\theta<\theta_{cr}$	7.10 E-03	1.07 E-01	$\theta<\theta_{cr}$	7.39 E-04	2.72 E-02	$\theta<\theta_{cr}$	1.77 E-04	1.20 E-02	$\theta<\theta_{cr}$
	1.5	2.83 E-03	7.98 E-03	4.99 E-01	5.53 E-01	$\theta<\theta_{cr}$	1.60 E-02	1.07 E-01	$\theta<\theta_{cr}$	1.66 E-03	2.72 E-02	$\theta<\theta_{cr}$	3.99 E-04	1.20 E-02	$\theta<\theta_{cr}$
366	1.5	2.83 E-03	7.98 E-03	4.99 E-01	5.53 E-01	$\theta<\theta_{cr}$	1.60 E-02	1.07 E-01	$\theta<\theta_{cr}$	1.66 E-03	2.72 E-02	$\theta<\theta_{cr}$	3.99 E-04	1.20 E-02	$\theta<\theta_{cr}$
	2.0	3.77 E-03	1.42 E-02	8.87 E-01	5.53 E-01	$\theta>\theta_{cr}$ erodible	2.84 E-02	1.07 E-01	$\theta<\theta_{cr}$	2.96 E-03	2.72 E-02	$\theta<\theta_{cr}$	7.10 E-04	1.20 E-02	$\theta<\theta_{cr}$

the flow velocity is greater than 1 m/s. At 25 r/min propeller rotation, the value of the water flow velocity is below 0.5 m/s for all depths. At 75 r/min, the maximum velocity value is up to 1 m/s for 0.5 D_p and 1.0 D_p depth. For rotation of 120 r/min, the maximum velocity value reaches 2 m/s for a depth of 0.5 D_p and 1.5 m/s for a depth of 1.0 D_p. For 230 r/min rotation , the maximum velocity value reaches 4 m/s at a depth of 0.5 D_p, 2.5 m/s at a depth of 1.0 D_p, 2 m/s at a depth of 1.5 D_p and 1.5 m/s at a depth of 2.0 D_p. At 366 r/min, the maximum velocity value reaches 6 m/s for 0.5 D_p depth, 5 m/s for 1.0 D_p depth, 3.5 m/s for 1.5 D_p depth and 2 m/s for 2.0 D_p depth. The potential for erosion is caused by the propeller rotation based on the type of seabed particles, as presented in Figure 12. The existing approaches show that for a vertical distance of 0.5 D_p from the propeller axis, the potential for erosion on all seabed particles can occur at all rotation quantities. If the vertical distance is more significant, the water flow from the propeller does not cause erosion for a certain amount of rotation and certain bottom conditions.

Table 5 shows potential map erosion based on propeller rotation, water depth, and seabed particle types. In line with previous research, the greater the propeller rotation and the closer the propeller is to the seabed, the easier the erosion process occurs. Figure 14 is compared with the UKC with the standards commonly used in shipping. The UKC value required by the propeller rotation threshold is least 20% of the ship's draft (T) at propeller rotation more than 100 r/min.

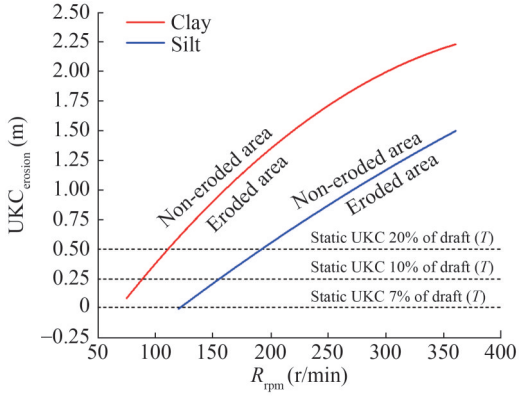

Figure 14 Threshold of UKC and propeller rotation for diameter (D_p=1.5 m) based on the seabed particle

5 Conclusions

This research determines the propeller rotation threshold based on the pressure of the water flow velocity on seabed particles by empirical approach, numerical simulation, and experimentation on a model scale. The rotation propeller with a diameter (D_p) of 1.5 m initiates the seabed erosion at the distance of the shaft axis to the seabed is 0.5D_p and rotation of 75 r/min for Clay particles, 120 r/min for Silt particles, 230 r/min for Sand and Gravel particle. If the distance from the axis to the seabed equals D_p, the seabed erosion will arise at 75 r/min for Clay particles, 230 r/min for Silt and Sand particles and 360 r/min for Gravel particles. The higher the distance of the propeller from the seabed, the higher the rotation required to initiate erosion, as shown in Figure 14. It is recommended that the LCT Type mini LNG Carrier with a propeller diameter of 1.5 m requires UKC > 20% of the ship's draft (T) to prevent seabed erosion. Proposing further research to determine the magnitude of erosion and sedimentation due to the propeller diameter variation and its impact on aquatic ecosystems.

Acknowledgement We appreciate all reviewers and editors for their valuable comments and directions. We are very grateful for the valuable contributions of the following colleagues, who were very helpful in preparing experiments in the laboratory: Putri Virliani, Dwi Wahyudi, Erlangga Satria Aidil Putra, Fadila Norasarin Erithe, and all members of the hydrodynamics laboratory.

Competing interest The authors have no competing interests to declare that are relevant to the content of this article.

References

Abdillah HN, Artana KB, Dinariyana AAB, Handani DW, Aprilia PW (2021) Study on the LNG distribution to bali–nusa tenggara power plants utilizing mini LNG carriers. IOP Conference Series: Materials Science and Engineering 1052(1): 012055. http://doi.org/10.1088/1757-899x/1052/1/012055

ANSYS Fluent (2018) ANSYS Fluent Tutorial Guide 18. 15317:Issue April, Canonsburg, PA: ANSYS Inc

Berger W, Felkel K, Hager M, Oebius H, Schale E (1981) Courant provoque par les bateaux protection des berges et solution pour eviter l'erosion du lit du haut rhin. P. I. A. N. C., 25th Congress, Section I-1. Edinburgh

Blaauw HG, van de Kaa EJ (1978) Erosion of bottom and sloping banks caused by the screw race of manoeuvering ships. Delft Hydraul. Lab., Delft

British Standard (2003) Maritime structures-part 1 : code of practice for general criteria. Code of Practice for General Criteria. BS 6349-1(196): 254

Carlton JS (2007) Marine propeller and propulsion. Elsevier Ltd. All Right Reserved, 2nd edition. http://books.elsevier.com

Cihan K, Doğu A, Yılmaz D, Ozan AY, Yıldız O, Sahin C (2022) Unconfined propeller jet scours on clay/sand mixtures. Ocean Engineering, 264(August). https://doi.org/10.1016/j.oceaneng.2022.112448

Corcoran MK, Sharp MK, Wibowo JL, Ellithy G (2016) Evaluating the mechanisms of erosion for coarse-grained materials. E3S Web of Conferences 7: 03008. http://doi.org/10.1051/e3sconf/20160703008

Crittenden JC, Trussell RR, Hand DW, Howe JK, Tchobanoglous G (2012) Research and Markets ; MWH's Water Treatment-Principles and Design. 3rd Edition. John Wiley & Sons, Inc, Hoboken

Cui Y, Lam WH, Zhang TM, Sun C, Hamill G (2019a) Scour induced by single and twin propeller jets. Water (Switzerland) 11(5):1097. https://doi.org/10.3390/w11051097

Cui Y, Lam WH, Zhang T, Sun C, Robinson D, Hamill G (2019b) Temporal model for ship twin-propeller jet-induced sandbed scour. Journal of Marine Science and Engineering, 7(10): 339. https://doi.org/10.3390/jmse7100339

Ferraro D, Aristodemo F, Lauria A, Lazzaro E, Pasquali D, Di Risio, M (2023) Effect of wave motion on the scouring caused by a marine propeller jet: An experimental and numerical study. Ocean Engineering, 290: 116426. https://doi.org/10.1016/j.oceaneng.2023.116426

Fuehrer M, Pohl H, Romisch K (1987) Propeller jet erosion and stability criteria for bottom protection of various construction. Bulletin of the Permanent International Association of Navigation Congresses [PIANC] 58:12. https://trid.trb.org/view/397304

Gotoh H, Khayyer A (2016) Current achievements and future perspectives for projection-based particle methods with applications in ocean engineering. Journal of Ocean Engineering and Marine Energy 2(3): 251-78. http//doi.org/10.1007/s40722-016-0049-3

Hamill GA (1988) The Scouring Action of The Propeller Jet Produced by a Slowly Manoeuvring Ship. Bulletin of the Permanent International Association of Navigation Congresses [PIANC] 62:85-110

Hamill GA, Johnston HT (1993) The decay of maximum velocity within the initial stages of a propeller wash. Journal of Hydraulic Research 31(5): 605-613. http://doi.org/10.1080/00221689309498774

Hamill GA, Kee C, Ryan D(2015) Three-dimension efflux velocity characteristics of marine propeller jets. Proceedings of the Institution of Civil Engineers: Maritime Engineering, 168(2): 62-75. https://doi.org/10.1680/jmaen.14.00019

Hashmi HN (1993) Erosion of a granular bed at a quay wall by a ship's screw wash. The Queen's University of Belfast, Northern Ireland

Hjulström F (1995) Transportation of detritus by moving water. Recent Marine Sediments, edited by Parker D Trask, vol. 4, SEPM Society for Sedimentary Geology. http://doi.org/10.2110/pec.55.04.0005

Hong J H, Chiew Y M, Cheng N S(2013) Scour caused by a propeller jet. Journal of Hydraulic Engineering, 139(9): 1003-1012. https://doi.org/10.1061/(ASCE)HY.1943-7900.0000746

Huai W, Yang L, Wang WJ, Guo Y, Wang T, Cheng Y (2019) Predicting the vertical low suspended sediment concentration in vegetated flow using a random displacement model. Journal of Hydrology, 578(September): 124101. https://doi.org/10.1016/j.jhydrol.2019.124101

Jiang JX, Lam WH, Cui YG, Zhang TM, Sun C, Guo JH, Ma YB, Wang SG, Hamill G (2019) Ship twin-propeller jet model used to predict the initial velocity and velocity distribution within diffusing jet. KSCE Journal of Civil Engineering 23(3): 1118-1131. http://doi.org/10.1007/s12205-019-1370-x

Kadir A, Istadi I, Iskendar I, Subadio A, Ali B, Nurcholis N, Waluyo W (2022) The operational concept of mini LNG carrier: preventing sedimentation on the seabed. IOP Conference Series: Earth and Environmental Science 1081(1): 012033. http://doi.org/10.1088/1755-1315/1081/1/012033

Kadir A, Istadi Subagio A, Iskendar I, Waluyo W, Kartikasari D, Palebangan H, Sadiah S, Himawan S, Virliani P, Kusuma Y F, Satria E, Putra A, Eritha F N (2023) The effect of the external counter rotating for the water flow velocity profile of twin propeller system. Journal of Applied Science and Engineering, 27(8): 2945-2955. https://doi.org/10.6180/Jase.202408_27(8).009

Kaidi S, Smaoui H, Sergent P (2021) Numerical investigation of the inland transport impact on the bed erosion and transport of suspended sediment: propulsive system and confinement effect. Journal of Marine Science and Engineering 9(7): 746. http://doi.org/10.3390/jmse9070746

Lam W, Hamil GA, Song YC, Robinson D, Raghunathan S (2011) A review of the equations used to predict the velocity distribution within a ship's propeller jet. Ocean Engineering 38(1): 1-10. http://doi.org/10.1016/j.oceaneng.2010.10.016

Legawa KSN, Artana KB, Pratiwi E (2020) Economic analysis of LNG distribution for power plant and city gas in bali. IOP Conference Series: Earth and Environmental Science 557(1): 012044. http://doi.org/10.1088/1755-1315/557/1/012044

Massey B (2006) Mechanics of Fluids. 8th ed. Revised by Ward-Smith John. New York: Taylor & Francis

Miedema SA (2013) Constructing the shields curve part C: cohesion by silt, hjulstrom, sundborg. Proceedings of the International Conference on Offshore Mechanics and Arctic Engineering Volume 6: Polar and Arctic Sciences and Technology; Offshore Geotechnics; Petroleum Technology Symposium. Nantes, France. http://doi.org/10.1115/OMAE2013-10524

Mohr H (2015) Erosion and Scour Behavior of Marine Sediments. The University of Western Australia (Issue April). Claremont: The University of Western Australia

Mujal-Colilles A, Gironella X, Crespo AJC, Sanchez-Arcilla A (2017) Study of the bed velocity induced by twin propellers. Journal of Waterway, Port, Coastal, and Ocean Engineering 143(5): 1-8. http://doi.org/10.1061/(asce)ww.1943-5460.0000382

Oud G, Bedos A (2022) CFD investigation of the effect of water depth on manoeuvring forces on inland ships. Journal of Ocean Engineering and Marine Energy 8(4): 489-497. http://doi.org/10.1007/s40722-022-00253-y

PIANC (1985) Underkeel clearance for large ships in maritime fairways with hard bottom. Report of a Working Group of the Permanent Technical Committee II, edited by PIANC, No 51, General Secretariat of PIANC

PIANC (2008) Considerations to Reduce Environmental Impacts of Vessels. In PIANC REPORT No 99 (Issue February). http://www.pianc.org

Schmunk C, Dogan M, Altun S (2023) Predicting propeller jet scour in silty and sandy marine environments. Ocean Engineering, 286(P1): 115558. https://doi.org/10.1016/j.oceaneng.2023.115558

Scully B, Young D (2021) Evaluating the underkeel clearance of historic vessel transits in the southwest pass of the Mississippi River. Journal of Waterway, Port, Coastal, and Ocean Engineering 147(5):1-13. http://doi.org/10.1061/(asce)ww.1943-5460.0000655

Shields A (1936) Turbulence Bed-Load 47

Soulsby R (1997) Dynamics of marine sands: a manual for practical applications 9:947. Telford. https://books.google.co.id/books?id=c-1OAAAAMAAJ

The Ministry of Energy and Mineral Resources of Republic of Indonesia (2021) Rencana Usaha Penyediaan Tenaga Listrik (RUPTL) PT PLN (Persero) 2021-2030. The Ministry of Energy and Mineral Resources of Republic of Indonesia

van Rijn LC (2007a) Unified view of sediment transport by currents and waves. III: graded beds. Journal of Hydraulic Engineering, 133(7): 761-775. https://doi.org/10.1061/(ASCE)0733-9429(2007)133:7(761)

van Rijn LC (2007b) Unified view of sediment transport by currents and waves, Part 1: initiation of motion, bed roughness and bed load transport. Jounal of Hydraulic Engineering, 133(6):649-667. http://doi.org/10.1061/(ASCE)0733-9429(2007)133:6(649)

van Rijn L, Kroon A (1993) Sediment transport by currents and waves. Proceedings of the Coastal Engineering Conference, 3:

2613-2628. https://doi.org/10.1061/9780872629332.199

Verhey H (1983) The Stability of Bottom and Bank Subjected to The Velocities in The Propeller Jet Behind Ships. International harbour Congress, 8th. Antwerp: TRB 11. https://trid.trb.org/view/394671

Wei MX, Chiew YM (2018) Characteristics of Propeller Jet Flow within Developing Scour Holes around an Open Quay. Journal of Hydraulic Engineering 144(7): 04018040. http://doi. org/10.1061/(asce)hy.1943-7900.0001470

Yang Y, Gap S, Wang YP, Jia JJ, Xiong JL, Zhou L (2019) Revisiting the problem of sediment motion threshold. Continental Shelf Research 187: 103960. http://doi.org/10.1016/j.csr.2019.103960

Yao WD (2019) An experimental study of scour around subsea structures. Perth: The University of Western Australia. http://doi.org/ 10.26182/5d1983cf4917b

Zhang AM, Li SM, Cui P, Li S, Liu YL (2023a) A unified theory for bubble dynamics. Physics of Fluids, 35(3): 033323 https://doi.org/10.1063/5.0145415

Zhang AM, Li SM, Cui P, Li S, Liu YL (2023b) Interactions between a central bubble and a surrounding bubble cluster. Theoretical and Applied Mechanics Letters, 13(3): 100438. https://doi.org/10.1016/j.taml.2023.100438